PHYSICAL REVIEW A **80**, 062902 (2009)

Highly charged Ar^{q+} ions interacting with metals

Jijin Wang, Jian Zhang, Jiangang Gu, Xianwen Luo, and Bitao Hu[*]
School of Nuclear Science and Technology, Lanzhou University, Lanzhou 730000, China
(Received 17 August 2009; published 10 December 2009)

Using computer simulation, alternative methods of the interaction of highly charged ions Ar^{q+} with metals (Au, Ag) are used and verified in the present work. Based on the classical over-barrier model, we discussed the promotion loss and peeling off processes. The simulated total potential electron yields agree well with the experiment data in incident energy ranging from 100 eV to 5 keV and all charge states of Ar^{q+}. Based on the TRIM code, we obtain the side-feeding rate as well as the motion and charge transfer of HCI below the surface. Some results, including the array of KL^x x-ray satellite lines, the respective contribution of autoionization, and side-feeding to inner shells, and the filling rates and lifetime of inner shells for Ar agree well with experiment or theory.

DOI: 10.1103/PhysRevA.80.062902 PACS number(s): 34.35.+a, 34.70.+e, 79.20.Rf, 32.30.Rj

I. INTRODUCTION

The interaction of slow highly charged ions (SHCIs, $v \ll 1$ a.u.) with metals has attracted much attention for decades for their strong electric fields and large potential energies [1–5]. As the SHCI approaches a metal surface, it induces a collective response of the surface electrons, creating an "image charge" which accelerates the SHCI. When the SHCI reaches the critical distance R_c, it can resonantly capture electrons from the states near the Fermi edge of metal surface to its high-lying Rydberg states and forms "hollow atom." This initial stage of SHCI-surface interaction seems to be well described by a classical over-barrier (COB) model [4], which is applicable above the surface. The main electron-transport pattern of COB model includes resonant capture (RC), resonant loss (RL), and autoionization ($\mathcal{A}$). The formation and decay of hollow atoms can make significant contribution to the total observable "above-surface" electron emission yields, namely, (i) autoionization of the multiply excited hollow atoms, due to its decay by cascade Auger or radioactive decay [4], (ii) promotion loss ($\mathcal{L}$) of electrons previously captured by the projectile due to their combined action of self- and image-charge screening near the surface, (iii) peeling off ($\mathcal{O}$) of all electrons still bounded in highly excited projectile states at the very moment of surface impact [6–8]. For the promotion loss, a classical criterion $\varepsilon_n > 0$ for electron emission is normally used. For the peeling off, theoretical description becomes more difficult due to the strong perturbation of the initial electron distribution of the metal surface and the intricate molecular dynamics and for the higher incident charge states, the detailed quantum-mechanical treatment is complicated and a first-principles approach remains a formidable task [9–12].

When SHCI reaches the solid surface, it may penetrate into or reflect from the solid. The high neutralization and relaxation of the reflected ions [13,14] and the array of KL^x x-ray satellite lines [3,15,16] cannot be explained by only the autoionization rates. Therefore, the side-feeding ($\mathscr{F}$) mechanism, which is now known as the direct transfer of electrons from target states into inner shells of ion, was proposed [17,18]. References [19,20] gave a multiple-cascade model for the inner-shell filling of HCI moving below the surface, in which the L-shell filling rates are evaluated by the molecular-orbital diagram [21], but the molecular orbits are difficult to calculate, especially for higher shells ($n > 2$) [19,20,44]. There were some discussions for $\mathscr{F}$ in some early papers [8,18], but the precise verifications in both experiment and theory for inner-shell $\mathscr{F}$ processes are still missing due to the complication of ion-atom collision below the surface.

The below-surface electron emission can be induced by the autoionization and the kinetic electrons (KEs) [22–27]. If a projectile has velocity as high as the threshold velocity v_{th}, the maximum energy transfer equals the work function and the ejection of kinetic electrons into vacuum happens.

In this paper, we presented a quantum solution for promotion loss and proposed a model for the peeling off to analyze carefully the complicated total electron yields of HCI interacting with metal surface. All charge states of Ar^{q+} in incident energy ranging from 100 eV to 5 keV are simulated to verify the whole physical processes in our code. The simulation results agree well with experiments [28–30]. We also simulated the x-ray emission spectrum of Ar^{q+} ($q = 17, 18$) in different incident energy interacting with various metal targets and calculated the electron filling speed and the lifetime of K and L shells below the surface [31–34] to prove the validity of our side-feeding methods. The simulated quantitative contribution of $\mathcal{A}$ and $\mathscr{F}$ below the surface, which to our knowledge have not been studied carefully, is also in a reasonable extent. The atomic units are used unless otherwise stated.

II. MODELING

Interaction force. The interaction of SHCI with solid surface is truly a many-body problem. An SHCI with charge state q_1 at a distance R from the solid surface is subjected from two forces

$$\vec{\mathcal{F}}(q,R) = \mathcal{F}_{im}\hat{e}_x + \sum \vec{\mathcal{F}}_{TFM}(R), \tag{1}$$

in which the first item is the image force, which always directs toward the surface, and can be given by

---

[*] Corresponding author; hubt@lzu.edu.cn

$$\mathcal{F}_{im}(R) = \frac{q_1(R)^2}{4R}, \tag{2}$$

and the second one is the sum of the forces experienced by SHCI from all target atoms. It can be calculated by equation

$$\vec{\mathcal{F}}_{TFM}(R) = \frac{d}{dR}[W_{TFM}(R)], \tag{3}$$

where the W_{TFM} is the Coulomb potential between projectile and a target atom. The interaction potential for atoms with atomic numbers Z_1 and Z_2 separated by a distance r can be approximated by screened Coulomb potentials of the type

$$W_{TFM} = \frac{Z_1 Z_2}{r}\phi(r/a_{\mathcal{F}}). \tag{4}$$

In Eq. (4), the $\phi(r/a_{\mathcal{F}})$ is an interatomic "screening function" [35] and $a_{\mathcal{F}}$ is the screening length

$$a_{\mathcal{F}} = \frac{0.8854}{\sqrt{(Z_1 - q_1)^{2/3} + (Z_2 - q_2)^{2/3}}}, \tag{5}$$

where q_1 and q_2 are the charge states of projectile and target atom, separately.

Charge exchange process. Within the critical distance R_c, charge transfer between HCI and solid surface occurs mainly through resonant and Auger processes. In our simulation, the Cowan code [36] was adopted to calculate the atomic Auger rate for $n > 3$ in vacuum

$$A_{nn'} = \frac{5.06 \times 10^{-3}}{|\Delta n|^{3.46}}, \tag{6}$$

where n is the main quantum number. For inner shells, the Auger rates in Refs. [18,37] were used. A theoretical analysis of the neutralization dynamics above the surface had been presented on the basis of the classical over-the-barrier model [4], including the resonant multielectron capture of conduction electrons, the resonant loss into unoccupied states of conduction band, and the intra-atomic Auger deexcitation. The following is a rate equation for the population P_n of n_{th} shell:

$$\begin{aligned} \frac{dP_n}{dt} &= \theta(S_n - P_n) I_n^{\text{RC}} - I_n^{\text{RL}} P_n + \theta(S_n - P_n) w_n^{fin} \sum_{n'>n} A_{n'n} w_{n'}^{ini} \\ &\quad - 2 w_n^{ini} \sum_{n'<n} A_{nn'} w_{n'}^{fin} - I_n^{\mathcal{O}} P_n + \theta(S_n - P_n) I_n^{\mathcal{F}}, \end{aligned} \tag{7}$$

where I_n^{RC} and I_n^{RL} are the current of resonant captured and lost electrons [4], $I_n^{\mathcal{O}}$ is the decay rate of $\mathcal{O}$ process, $I_n^{\mathcal{F}}$ is the electron-capture rate of $\mathscr{F}$process, w_n^{ini} and w_n^{fin} are the (empirical) statistical factors to correct the auger rate $A_{n'n}$ [Eq. (6)], S_n is the number of electrons fully filled of n_{th} shell, and θ is the unit step function.

A. Promotion loss

One important process which is missed in Eq. (7) but actually switched on in our physical model is the promotion loss process. The classical model for $\mathcal{L}$ can be explained by the electron energy level, which is expressed as [4]

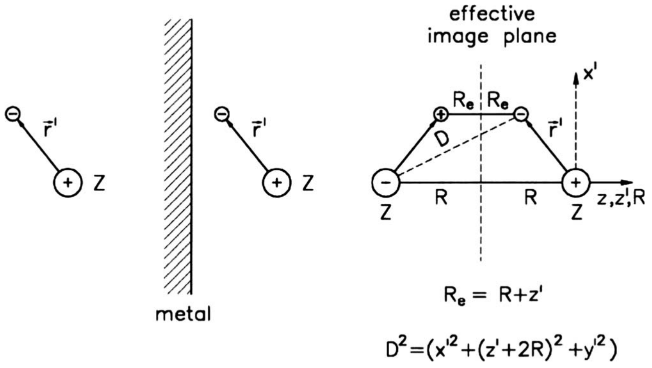

FIG. 1. Sketch of image-charge interaction of an atom in front of metal surface.

$$\varepsilon_n = -\frac{q_n^2}{2n^2} + \frac{q - 1/2}{2R}. \tag{8}$$

In Eq. (8), q_n is the effective charge state of projectile ion felt by an electron on the n_{th} shell, which can be calculated by the Slater rule [38], and q is the charge state of the ion at distance R. The first term of Eq. (8) is atomic energy level of n_{th} shell, which is modified by the second term caused by the self-image charge of HCI. When the HCI approaches to metal surface, the projectile energy levels ε_n will be shifted upwards due to the screening of the already captured electrons and the repulsive interaction of self-image of HCI, i.e., the action of the first and second terms in Eq. (8). With the decrease of q_n and R, ε_n will be larger than zero at a certain distance and electrons on n_{th} shell can escape into vacuum, which is called promotion loss electrons. In this paper, the quantum perturbation theory is used and the $\mathcal{L}$ electron emission will no longer be decided by the critical vacuum level $\varepsilon = 0$ but the quantum emission rates.

In Fig. 1, the HCI–outer-shell electron is regarded as a hydrogenlike ion. On the left side, a free atom with single active electron outside an ion core with effective charge Z is sketched. The Hamiltonian for this problem is

$$H_a = \frac{\nabla^2}{2} - \frac{Z}{r'}, \tag{9}$$

where the atomic frame is denoted by primed coordinates [35].

In the vicinity of a conducting surface plane, the active electron is perturbed. This perturbation is treated with the concept of image charges (right part of Fig. 1) by taking into account the interaction of the electron with its own image charge and the image charge of the ion core. We introduce a coordinate R for the position of the atomic core along z, referred to the electronic image plane [59], i.e., $R = z - z_{\text{im}}$.

The image charges of electron and ion cores cause an additional potential term H_p in the Hamiltonian

$$H = H_a + H_p = \frac{\nabla^2}{2} - \frac{Z}{r'} + \frac{Z}{D} - \frac{1}{4R_e}, \tag{10}$$

where the distances D and R_e are given in Fig. 1. Expansion of H_p in powers of $1/R$ yields

$$\begin{aligned} H_p = H' = {} & \frac{2Z-1}{4R} - (Z-1)\frac{z'}{4R^2} + \left[\left(\frac{3}{4}Z-1\right)z'^2 - \frac{Z}{4}r^2\right]\frac{1}{4R^3} \\ & + \left[\frac{3}{8}Zr^2 - \left(\frac{5}{8}Z-1\right)z'^2\right]\frac{z'}{4R^4} + O\left(\frac{1}{R^5}\right), \end{aligned} \tag{11}$$

where $z' = r\cos(\theta)$. With the hydrogenlike model, the initial-state wave function $\Psi_n^{(0)}$ can be got. Using first approximation of stationary-state perturbation theory, the final-state wave function of electron on outmost shell of HCI is

$$\begin{aligned} \Psi_n = \Psi_n^{(0)} + \Psi_n^{(1)} = \Psi_n^{(0)} + \sum_k{}' \frac{H'_{kn}}{E_n^{(0)} - E_k^{(0)}}\Psi_k^{(0)} (n \\ = 1,2,3\ldots,\quad k = 1,2,3\ldots,\quad n \neq k), \end{aligned} \tag{12}$$

where

$$H'_{kn} = \int \Psi_k^{(0)} H' \Psi_n^{(0)} d\tau', \tag{13}$$

$$H' = \frac{2Z-1}{4R} - (Z-1)\frac{r\cos(\theta)}{4R^2} \tag{14}$$

is the secondary approximation of Hamiltonian H_p and n is the main quantum number. Since when $|n-k| > 4$, $H'_{kn} \ll E_n^{(0)} - E_k^{(0)}$, so $k = n-2\ldots n+4$ is adopted.

The emitted electron is regarded as free electron with the time-independent stationary-state plane-wave function $e^{i\vec{p}\cdot\vec{r}/\hbar}$. The emission rate of electron from bound state of outer shell to free state can be expressed as

$$\begin{aligned} \Gamma = \left|\int \Psi_n e^{i\vec{p}\cdot\vec{r}/\hbar} d\tau\right|^2 = \Bigg|\int \Bigg(\Psi_n^{(0)} \\ + \sum_k{}' \frac{\int \Psi_k^{(0)} H' \Psi_n^{(0)} d\tau'}{E_n^{(0)} - E_k^{(0)}}\Psi_k^{(0)}\Bigg) e^{i\vec{p}\cdot\vec{r}/\hbar} d\tau\Bigg|^2. \end{aligned} \tag{15}$$

Therefore, the emission rate in unit time is obtained as

$$I = \Gamma N P, \tag{16}$$

where N is the possible $\mathcal{L}$ electron number obtained from simulation and P is the proportion of HCI volume below the surface to whole volume.

If an electron is emitted through $\mathcal{L}$ process, it can leave metal surface and can be detected only when $E_e > U_{im}$. E_e is the electron kinetic energy and U_{im} is the potential energy of emitted electron induced by electron self-image charge [39]

$$U_{im} = \begin{cases} \dfrac{1}{4R}, & R \geq 5 \\ \dfrac{1}{4(1.025 + 0.9946R + 5.253^{-5}R^2)}, & R < 5, \end{cases} \tag{17}$$

where R is the distance between HCI and surface image plane. In our calculation, if R is smaller than 5, the second formula of Eq. (17) is adopted.

B. Peeling off

With the HCI approaching the surface, the outer shells are continually populated with weak binding energy and large orbital radius (comparable to the critical electron resonant capture distance R_c). Electrons in these shells will interact with metal surface. It is assumed that when $R < r_n + z_j - \lambda_{scr}$ [8], the outer orbital electrons of HCI are likely to move to valence-band continuum if their classical radii r_n exceed the screening length λ_{scr}, where R is distance between HCI and image plane of surface and z_j is the average distance from jellium edge to the first atom surface [59]. These electrons may be peeled off by the target atoms or stop in target for the electron stopping power of target electron gas. If they are not peeled off, they will return to original orbit of HCI.

The peeling off rates for outer-shell electrons were difficult to calculate due to the strong perturbation of target surface electron gas and complexity of bound outer-shell orbital electrons of HCI. Some early papers provided the $\mathcal{O}$ emission rates, which are expressed as orbital period times target material density and target-HCI interaction orbital length [8,40]. To obtain the $\mathcal{O}$ cross section, in the present work we used the $\mathcal{O}$ cross section, which is the product of the screened Rutherford scattering cross section σ_{sn} for free electrons colliding with target atoms [41,42] and the modification factor $\mathcal{F}(E_0)$, modifying σ_{sn} for the bounded electron. The emission rate of $\mathcal{O}$ electron is expressed as

$$I_n = \nu_n L N \sigma_{sn} \mathcal{F}(E_0), \tag{18}$$

where ν_n is electron orbital frequency, L is the overlapped orbital length of HCI and target, N is the density of target atom, E_0 is the energy level of outer-shell electrons, and n is the main quantum number. The screened Rutherford scattering cross section σ_{sn} in the present work is expressed as

$$\sigma_n = \frac{d\sigma(\theta)}{d\theta} = K_n \frac{Z^2}{E^2} \frac{\sin\theta}{4(1 + 2\beta - \cos\theta)^2}. \tag{19}$$

In Eq. (19), β is screening parameter

$$\beta = k\frac{Z^{2/3}}{E}, \tag{20}$$

where θ is scattering angle ($d\Omega = 2\pi \sin\theta d\theta$), $K_n = (\pi e^4/2)$, and $k = (e^2/8a_0)$. Ω is the solid angle, a_0 is the Bohr radius of hydrogen, and E is the kinetic energy of incident electron.

For most authors, in the secondary-electron (SE) energy range ($E \approx 10-100$ eV), the potential around each ion is central. A screened Rutherford cross section has sometimes been used, though it is only strictly valid for higher energies [41]. The present simulation used the σ_{sn} for free electrons and used the modification factor $\mathcal{F}(E_0)$ for bound electrons, which will be discussed in Sec. III. After the scattering processes, electrons will be stopped or attenuated by the target electron gas below the surface. To simulate the motion, an attenuation function is adopted [22]

$$f = \exp(-x/L), \tag{21}$$

where x is the traveled path length of electrons in target and L (nm) is the mean-free path (MFP) of electron moving in solid [43,49]

$$L = \frac{538a}{E^2} + 0.41a^{3/2}E^{1/2}, \tag{22}$$

where E (eV) is the electron energy and a (nm) is the monolayer thickness given by

$$a^3 = \frac{A}{\rho n N} \times 10^{24}, \tag{23}$$

where A is the atomic or molecular weight, n is the number of atoms in the molecule, N is the Avogadro's number, and ρ is the bulk density in kg m^{-3}. If electrons are less disturbed by target atoms or electron gas, it can return to the initial orbit.

C. Side-feeding

When the HCI collides with surface atoms or penetrates the surface, there is no enough time for the fulfilling of inner shells of HCI due to the low Auger deexcitation speed and the acceleration of HCI self-image charge above the surface. At this time, the $\mathscr{F}$ will play a more important role in the inner-shell electron capture. The $\mathscr{F}$, first observed by Folkerts and Morgenstem [50], is inner-shell electron transition between target and projectile, which can only take place in close collisions with the level crossing of inner shells between HCI and atoms. A physical description for $\mathscr{F}$ by molecular coulumb over-barrier (MCOB) model is given in Sec. III. Some early references [18,44] had given a basic $\mathscr{F}$ filling rate

$$\Gamma_n = n_c v \sigma_n, \tag{24}$$

where the n-shell charge-transfer cross sections σ_n are multiplied by target atoms density n_c and projectile velocity v. Based on Eq. (24), we gave a detailed $\mathscr{F}$ filling rate for inner shells

$$\Gamma_n = \Gamma_0 B_n n_c q_n N_{ol} v \sigma_n, \tag{25}$$

where Γ_0=2.39 is a fitting number, B_n the is standard Pauli blocking factor of a quantum Boltzmann collision term $B_n = (1-P_n/2n^2)$ in terms of a number of available unoccupied final states [45]. q_n is the effective charge state, N_{ol} is the proportion of HCI volume below the surface to whole volume, and the electron-capture cross section of n shell is given by

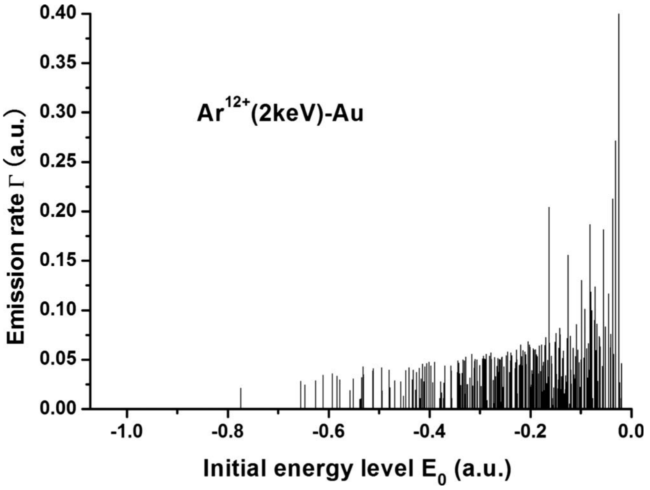

FIG. 2. $\mathcal{L}$ electron emission rates for 2 keV Ar^{12+} ions impinging on a gold surface vs the initial electron energy level.

$$\begin{aligned} \sigma_n &= \pi(r_n^2 - r_{n-1}^2) \\ &\ldots\ldots \\ \sigma_1 &= \pi r_1^2, \end{aligned} \tag{26}$$

where r_n is radius of n shell. The verification of the formula will be discussed in Sec. III.

D. Kinetic electron

The metal electrons (mass m_e) may be considered as freely moving with velocities of up to Fermi velocity $v_{\mathcal{F}}$. Then the maximum energy transfer ΔE from a projectile ion (velocity v) in a head-on collision is given by [22,46]

$$\Delta E = 2m_e v(v + v_{\mathcal{F}}). \tag{27}$$

When $\Delta E \geq W$, W is the work function of metal surface, the ejection of an electron into vacuum happens (kinetic electron). The KE threshold velocity v_{th} of incident projectile is given by

$$v_{\text{th}} = -\frac{v_{\mathcal{F}}}{2} + \left(\frac{v_{\mathcal{F}}^2}{4} + \frac{W_\Phi}{2m_e}\right)^{1/2}. \tag{28}$$

III. RESULTS AND DISCUSSION

A. Electron yields

In our simulation, if the classical criterion $\varepsilon_n > 0$ for Promotion loss is used [8], where ε_n is electron energy level, the total electron yields will be much larger than experiment results [30] due to the large $\mathcal{L}$ electron yields. So the quantum methods discussed in Sec. II was adopted.

In Fig. 2, the calculated $\mathcal{L}$ emission rates Γ ranges from 0 to 0.4 and electrons in a lighter bound state will be emitted easier; electrons with energy level below −0.6 are hardly to shift. Because the wave-function calculations will spend much CPU time, we simplify Eq. (15) and obtain numerically approximative formula for $\mathcal{L}$ emission rates

$$\Gamma = -\frac{C_0}{E_0} + C_1 \frac{n}{R^2 E_0^2}, \tag{29}$$

which is proved to agree well with the quantum calculation

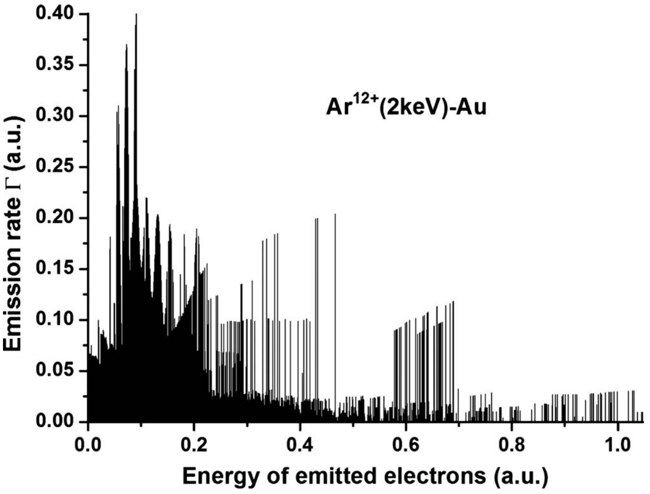

FIG. 3. $\mathcal{L}$ electron emission rates for 2 keV Ar^{12+} ions impinging on a gold surface vs emitted electron energy.

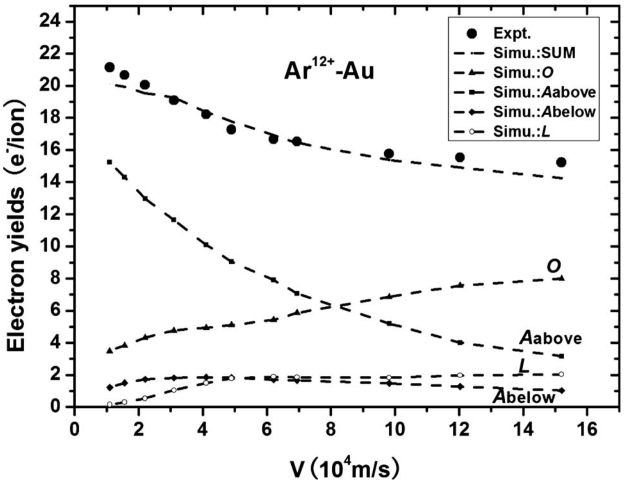

FIG. 4. Electron yields of Ar^{12+} ions impinging on Au surface with various velocities in normal incidence.

method in our simulation. $C_0=0.002$ and $C_1=0.0004$ are fitting numbers, E_0 is the energy level of initial electron state, and R is the distance between HCI and metal image plane. Figure 3 is $\mathcal{L}$ electron emission rates Γ versus final electron energy E for 2 keV Ar^{12+} ions colliding with Au target. The major contribution to emission rates comes from electrons with final energy ranging from 0.05–0.3 a.u.

For the complication of $\mathcal{O}$ mentioned above, the emission rate of it cannot be calculated with methods as same as $\mathcal{L}$ because for $\mathcal{O}$, the outer electrons are scattered by the target instead of the image charge which will largely increase the difficulty of calculation. Here, the cross section of $\mathcal{O}$ is treated by means of the calculated $\mathcal{L}$ emission rates. Because $\mathcal{O}$ and $\mathcal{L}$ are both scattering of bounded outer-shell electrons into vacuum, with target atoms and image charge of HCI, respectively, there should be a similar function form for their emission rates versus initial electron energy level. We can treat the function form of emission rates versus initial electron energy level of $\mathcal{O}$ with the function form of $\mathcal{L}$ in Fig. 2, which can be expressed as

$$\mathcal{F}(E_0) = \exp(CE_0), \tag{30}$$

where $C=2.3$ is adopted as a fitting number. $\mathcal{F}(E_0)$ equals to 1 for free electrons and approximates to 0 for heavy bounded electrons. In Eq. (18), the screened Rutherford scattering cross section σ_{sn}, used for free electron colliding with target atoms, times modification factor $\mathcal{F}(E_0)$ modifying σ_{sn} for the bounded electron to obtain the cross section of $\mathcal{O}$. With these electron transfer methods, we can simulate the total electron yields for Ar^{q+} ions colliding with Au surface.

For interaction of Ar ions with Au target, there are no kinetic electrons if incident velocities of Ar ions are below $v_{\text{th}}=0.112$ a.u. (for Au). Figures 4 and 5 show potential electron yields of experiment [30] and simulation results with incident kinetic energy ranging from 25 eV to 5 keV. For $\mathcal{A}$, $\mathcal{O}$, and $\mathcal{L}$, because 50% electrons are emitted toward the vacuum and the other 50% toward the target surface, the total detectable electron yields should be halved: $\Sigma=0.5(\mathcal{A}_{\text{above}}+\mathcal{A}_{\text{below}}+\mathcal{O}+\mathcal{L})$, where $\mathcal{A}_{\text{above}}$ is autoionization electrons emitted above the surface and $\mathcal{A}_{\text{below}}$ is the $\mathcal{A}$ electrons escaped from target. $\mathcal{O}$ and $\mathcal{L}$ are electron yields for peeling off and promotion loss, respectively. In Fig. 4, $\mathcal{A}_{\text{above}}$ occupies the major part of total yields, especially for very low incident energies (25 eV–1 keV), then gradually decreases with the increasing of incident velocity because when the incident velocity increases, there is less time for $\mathcal{A}$ above the surface. But $\mathcal{O}$ yields increase since there are more and

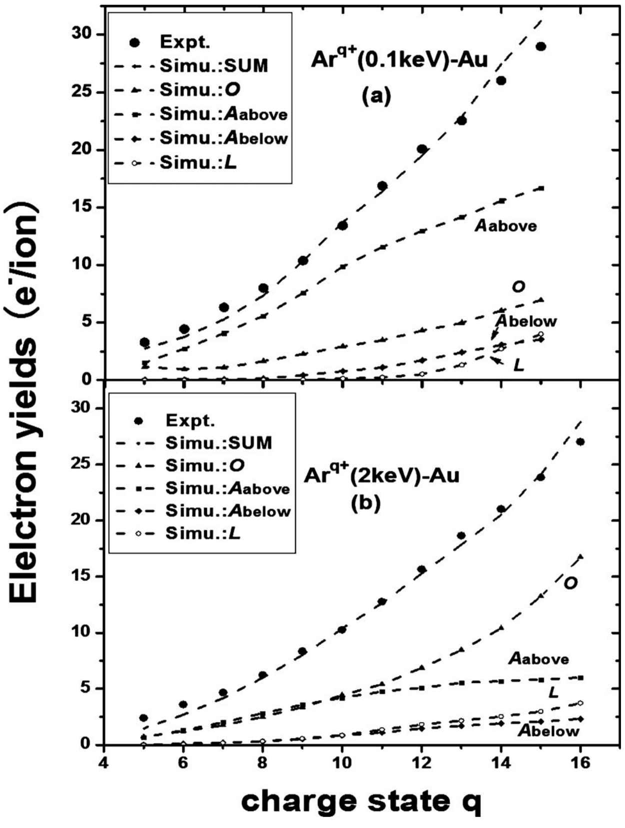

FIG. 5. Electron yields of (a)0.1 keV/(b)2 keV Ar^{q+} ions impinging on Au surface with various charge state in normal incidence.

more weakly bound electrons which can be peeled off in outer orbit. The $\mathcal{L}$ yields account for less than 5% of the total value and increase for the reason as same as $\mathcal{O}$. The emission of $\mathcal{A}$ electrons below the surface can also be obtained using Eqs. (21)–(23). These yields range from 1 to 2 and the maximum is at the incident velocity of 2.2×10^4 m/s. Figure 5 shows electron yields of 0.1 and 2 keV Ar ions impinging on Au surface with various charge states in normal incidence. All kinds of yields increase with the raising of charge state. At incident energy of 0.1 keV, $\mathcal{A}$ occupies the main part of total yields for there are more time for autoionization and more electrons de-excite to lower energy level. When incident energy is at 2 keV, HCI has less time above the surface and $\mathcal{O}$ yields are about the same as $\mathcal{A}$ at charge states below 10 and contribute more to the total yields at higher charge states. The electrons of very low energy ($E<10$ eV), which are absorbed by metal surface, share about 2%–8% of the total electron yields for 0.1–5 keV incidence. The KEs cannot be emitted if incident ion velocities are below v_{th} (for Au, Ag, $v_{\mathrm{th}}=0.112$, 0.105 a.u., $E_{\mathrm{th}}=12.43$, 10.9 keV), so there are no KE yields in Figs. 4 and 5.

B. X-ray emission

X-ray spectrum is very important for us to study the inner-shell charge exchange for its clock property [48], involving the matching between energy of x-ray lines and the electron distribution of atom while de-exciting. When Ar^{q+} ions interact with metal surface, hollow atom is formed above the surface. The M (or N) shells are filled up when the HCI enters the solid surface. L shell is fed more slowly mainly via Auger transitions. The KL^x lines, which are observed during the filling of K hole, occur in the presence of a certain number of L spectator electrons and form a characteristic array of satellite lines corresponding to each of the transitions with any number x of L spectator electrons. The eight KL^x lines, which display the step-by-step filling of the L shell ($KL^1-KL^2-\cdots$), have been used to study the decay of hollow atoms [15]. The energy of KL^x lines is calculated by formulas [18,37]

$$\begin{array}{l} E_{K\alpha}=3144.3-22.2n_L-4.9n_M+0.4n_Ln_M \\ E_{K\beta}=3702.4-60.7n_L-15.9n_M+1.5n_Ln_M \end{array} \text{(eV)}. \qquad (31)$$

The $\mathcal{T}$ process is known as the direct transfer of electrons from target into inner shells of HCI. Burgdorfer *et al.* [6] gave the $\mathcal{T}$ rates above the surface for HCI impinging on metal surface in grazing incidence within the over-barrier model. For the rates below the surface, the multiple-cascade model and the molecular-orbital diagram were given to describe the electrons exchanging between various shells below the surface, but the molecular orbits are difficult to calculate. According to the evaluation in Ref. [34], a small part ($\leq30\%$) of the L holes of HCI is filled by $\mathcal{T}$ processes; the geometrical cross section for capturing electrons into the M and N shells of the ion is much larger than into the L shell ($\sigma\sim n^4$).

A physical diagram which can describe $\mathcal{T}$ process is the MCOB model [51,52]. When the ion moves closer to atom, the potential barrier between ion and atom will be brought down, some outer orbital electrons are shared by two cores, and the molecular orbits form. When the distance between the two cores becomes the smallest, most electrons are in molecular orbits. Then two cores are separated and electrons in molecular orbits return to the ion or atom. The detailed returning rates, shell numbers, and energy levels electrons can be calculated by the shell-electron population of the ion and atom within the MCOB model. Through this method, maybe the detailed $\mathcal{T}$ process can also be obtained within an inner-surface environment, which is approximatively a mean electron-gas field.

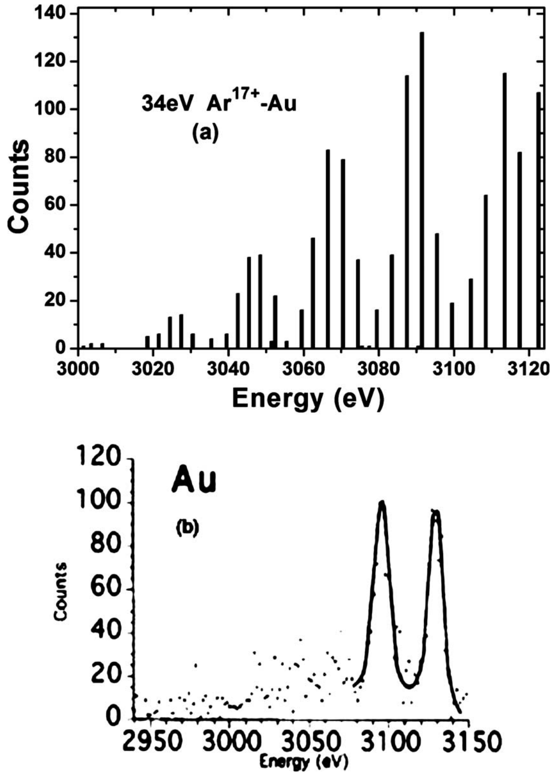

FIG. 6. The (a) simulation and (b) experiment [47] results of KL^x x-ray satellite line spectra of 34 eV Ar^{17+} impinging on Au in normal incidence.

When HCI collides with target surface, considering the matching of energy level, only the shells of which energy level is lower than metal Fermi level can get electrons through $\mathcal{T}$ mechanism. $\mathcal{T}$ is a collision electron transfer process, so the HCI in grazing incidence will obtain more $\mathcal{T}$ electrons than which in normal incidence. When HCI is very close to or has collided with first target atom plane, it will be surrounded by target electron gas quickly. The N shell and higher orbits, particularly the continuum orbits, are treated together as one shell labeled C [53], so only the inner shells (K,L,M) for $\mathcal{T}$ processes are important. By the TRIM code, adding the $\mathcal{A}$ and $\mathcal{T}$ processes, we could obtain the charge transfer of HCI and the x-ray emission spectra below the surface following ion trace and energy.

Figure 6 shows the array of x-ray satellite lines of 34 eV Ar^{17+} impinging on Au in normal incidence. Because the incident energy is very low (34 eV), x ray is mainly generated when HCI is above or in the first several atom layers. The penetration of atom layer at a low velocity is caused for

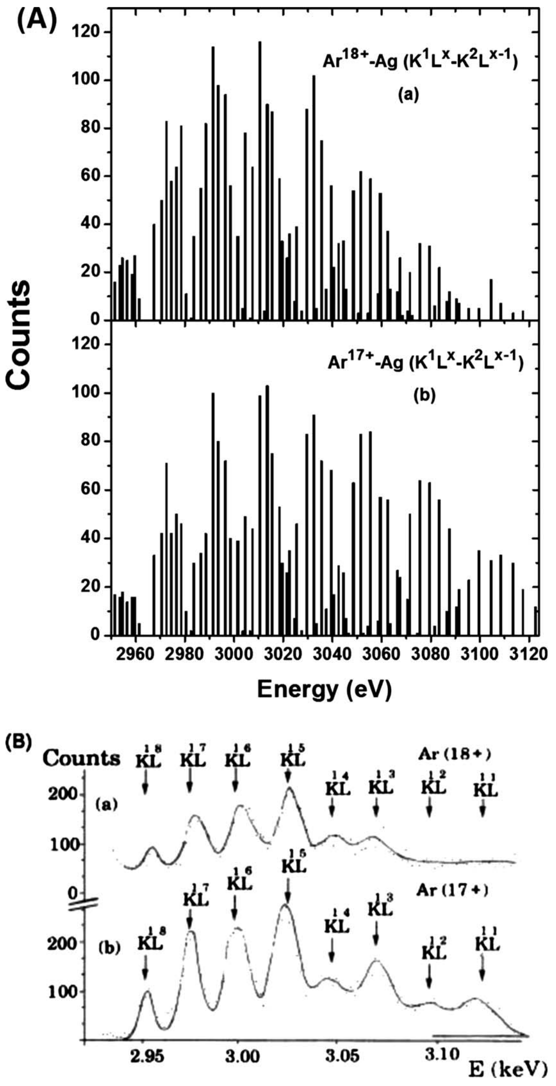

FIG. 7. The (A) simulation and (B) experiment [15] results of KL^x x-ray satellite lines spectrum ($K^1L^x - K^2L^{x-1}$) of (a) 359 keV Ar^{18+} and (b) Ar^{17+} impinging on Ag in normal incidence.

the reason of image acceleration [54–56]. In Eqs. (24) and (25), $\mathscr{F}$ rate is proportional to the velocity of projectile and because $\mathscr{F}$ is a collision electron-capture process, it will be low when HCI is not close to target atoms. So in low incident energy 34 eV, electrons are captured to outer orbits mainly through RC process. Due to the low $\mathcal{A}$ and RC speeds, inner shell of HCI will not be filled quickly and KL^x x ray will be generated in a low number (1–2) of L-shells spectator electrons. Figure 7 show the array of x-ray satellite lines of 359 keV Ar^{q+} ions impinging on Ag in normal incidence. Both (a) and (b) are x-ray emissions of $K^1L^x - K^2L^{x-1}$. The large incident energy (359 keV) will cause large $\mathscr{F}$ rates, so inner shells are filled quickly and KL^x x rays will be generated in a higher number (5–7) of L-shell spectator electrons. In Figs. 6 and 7, all the simulated x-ray spectra in different incident energy, charge state, and target agree well with the experiment results.

TABLE I. Average contribution of various electron-capture processes to inner shells (K,L,M) for 359 keV Ar^{18+} impinging on Ag.

	$\mathcal{A}$	$\mathscr{F}$	Loss($\mathcal{A}$)	X ray
K	1.60	0.09	0	0.31
L	8.14	2.08	2.06	
M	4.06	18.46	14.82	

For the large $\mathscr{F}$ electron transfer rates below the surface, the proportion of $\mathcal{A}$ rates to $\mathscr{F}$ is important. Table I is the simulated average contribution of various electron-capture processes to inner shells for 359 keV Ar^{18+} ion impinging on Ag [Fig. 7(a)]. In Table I, $\mathcal{A}$ and $\mathscr{F}$ are the main ways of filling. There are few $\mathscr{F}$ electrons for K-shell filling because of the very small cross section. The outer shells have larger $\mathscr{F}$ cross sections, M shell obtains 18.46 $\mathscr{F}$ electrons, but L shell obtains only 2. The "Loss($\mathcal{A}$)" means the lost average electron number due to the $\mathcal{A}$ emission. From Ref. [18], the transition rates for KLL and $K\alpha$ are $\Gamma = 3.18 \times 10^{-4}(2 - n_K)n_L(n_L - 1)\Theta(n_L - 2)$ and $\Gamma = 3.04 \times 10^{-4}(2 - n_K)n_L\Theta(n_L - 1)$, respectively, where n_K and n_L are the electron numbers of K and L shells and $\Theta(n_L - x)$ is the step function. Concerning the sum de-excitation rates of Auger and x ray to K shell, the proportion of filling contribution by Auger (1.60) to by x ray (0.31) agrees well with the proportion of KLL to $K\alpha$ rates in the average L spectator electron number $\langle n_L \rangle = 4 - 5$ for Fig. 7(a).

The two spectra in Fig. 8 clearly reflect the atomic clock

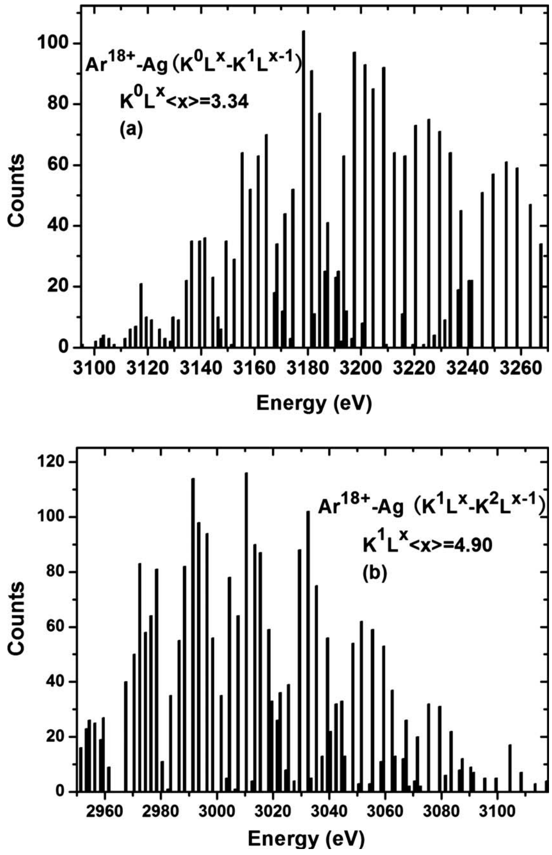

FIG. 8. The simulation results of KL^x x-ray satellite lines spectrum of 359 keV Ar^{18+} impinging on Ag (a) $K^0L^x - K^1L^{x-1}$ and (b) $K^1L^x - K^2L^{x-1}$ in normal incidence.

property of KL^x x-ray satellite lines. (a) and (b) are x-ray spectra with empty K shell and one electron-filled K shell with the average electron number of L shell $\langle x \rangle = 3.34$ and $\langle x \rangle = 4.90$, respectively. The number of electrons in L shell increases by $4.90 - 3.34 = 1.56$ and one electron de-excites from L to K. So at the time ranging that K shell obtains one electron, L shell obtains $1.56 + 1 = 2.56$ electrons, which agree well with Ref. [33]. Though there are some $\mathscr{F}$ electrons for L shell, the main way of filling is Auger de-excitation. The time between the first and second electron fillings of K shell, i.e., the life time of K^1L^{4-5}, is of the order of 10^{-15} s [37,57]. The mean time for filling a L hole, with mean $n_L = 4.5$ L spectator electrons and n_M M spectator electrons ($n_M > n_L$), is about $10^{-15}/2.56(\mathrm{s}) = 3.9 \times 10^{-16}$ s, which agrees with the theoretical estimates for the lifetime of LMM [57,58], so the electron transfer of HCI below the surface can be obtained through the atomic Auger transition and the $\mathscr{F}$ processes. The results in the present paper that about 25% of the L holes of HCI is filled by $\mathscr{F}$ processes and the geometrical cross section for capturing electrons into the M and N shells of the ion is much larger than into the L shell ($\sigma \sim n^4$) all agree with the evaluation in Ref. [34]. Figures 6–8 are also verifications for $\mathscr{F}$ rate formulas Eqs. (24) and (25). There are some deviations in energy of KL^x satellite lines between experiment and calculation, since Eq. (31) does not consider the influence of N or higher orbit electrons and target environment to atomic energy level.

IV. CONCLUSIONS

The present work involving the interaction of HCI with metals (Au, Ag) simulates the whole life of HCI, which mainly includes two aspects: above and below the surface processes. In the first part, the screened Coulomb potential and the over-the-barrier model is used to simulate the motion and charge-exchange processes. With the quantum solution for promotion loss and the modified model for the peeling off, simulated results of potential electron yields agree well with experiment results. In the second part, based on TRIM code, we add the charge transfer, including autoionization and side-feeding processes. By the charge-transfer rates below the surface, we simulated the array of x-ray satellite lines and the various contributions of electron filling to inner shells. The x-ray satellite lines are of atomic clock property, which will show the electron distribution while x ray is generating. Using these properties, the filling rates to inner shells and the lifetime of excited states are discussed. The $\mathscr{F}$ process is also discussed with the MCOB model, by which, adding some approximations of inner metal environment assumption, a more exact calculation for the $\mathscr{F}$ process is expected.

ACKNOWLEDGMENTS

This work is supported by the National Natural Science Foundation of China under Grant No. 10605011

---

[1] U. A. Arifov *et al.*, Sov. Phys. Tech. Phys. **18**, 240 (1973).
[2] E. D. Donets, Nucl. Instrum. Methods Phys. Res. B **9**, 522 (1985).
[3] J. P. Briand, L. de Billy, P. Charles, S. Essabaa, P. Briand, R. Geller, J. P. Desclaux, S. Bliman, and C. Ristori, Phys. Rev. Lett. **65**, 159 (1990).
[4] J. Burgdörfer, P. Lerner, and F. W. Meyer, Phys. Rev. A **44**, 5674 (1991).
[5] For recent review works, see *The Physics of Multiply and Highly Charged Ions*, edited by F. J. Currell (Kluwer Academic Publishers, Dordrecht, 2003), Vols. 1 and 2.
[6] J. Burgdörfer, C. Reinhold, and F. W. Meyer, Nucl. Instrum. Methods Phys. Res. B **98**, 415 (1995).
[7] H. Kurz, K. Toglhofer, H. P. Winter, F. Aumayr, and R. Mann, Phys. Rev. Lett. **69**, 1140 (1992).
[8] J. Ducree, H. J. Andra, and U. Thumm, Phys. Rev. A **60**, 3029 (1999).
[9] U. Wille, Nucl. Instrum. Methods Phys. Res. B **100**, 303 (1995).
[10] A. G. Borisov, R. Zimny, D. Teillet-Billy, and J. P. Gauyacq, Phys. Rev. A **53**, 2457 (1996).
[11] P. Kürpick and U. Thumm, Phys. Rev. A **54**, 1487 (1996).
[12] P. Nordlander, Phys. Rev. B **53**, 4125 (1996).
[13] S. Winecki, M. P. Stöckli, and C. L. Cocke, Phys. Rev. A **56**, 538 (1997).
[14] F. W. Meyer, L. Folkerts, and S. Schippers, Nucl. Instrum. Methods Phys. Res. B **100**, 366 (1995).
[15] J.-P. Briand, L. de Billy, P. Charles, S. Essabaa, P. Briand, R. Geller, J. P. Desclaux, S. Bliman, and C. Ristori, Phys. Rev. A **43**, 565 (1991).
[16] J.-P. Briand, S. Thuriez, G. Giardino, G. Borsoni, V. Le Roux, M. Froment, M. Eddrief, C. de Villeneuve, B. d'Etat-Ban, and C. Sébenne, Phys. Rev. A **55**, R2523 (1997).
[17] H. J. Andrä, A. Simionovici, T. Lamy, A. Brenac, G. Lamboley, J. J. Bonnet, A. Fleury, M. Bonnefoy, M. Chassevent, S. Andriamonje and A. Pesnelle, Z. Phys. D: At., Mol. Clusters **21**, 135 (1991).
[18] S. Winecki, C. L. Cocke, D. Fry, and M. P. Stöckli, Phys. Rev. A **53**, 4228 (1996).
[19] N. Stolterfoht, A. Arnau, M. Grether, R. Köhrbrück, A. Spieler, R. Page, A. Saal, J. Thomaschewski, and J. Bleck-Neuhaus, Phys. Rev. A **52**, 445 (1995).
[20] R. Page, A. Saal, J. Thomaschewski, L. Aberle, J. Bleck-Neuhaus, R. Kohrbruck, M. Grether, and N. Stolterfoht, Phys. Rev. A **52**, 1344 (1995).
[21] A. Arnau, R. Köhrbrück, M. Grether, A. Spieler, and N. Stolterfoht, Phys. Rev. A **51**, R3399 (1995).
[22] R. A. Baragiola, E. V. Alonso, and A. Oliva Florio, Phys. Rev. B **19**, 121 (1979).
[23] B. Svensson, G. Holmén, and A. Burén, Phys. Rev. B **24**, 3749 (1981).
[24] J. Ferrón, E. V. Alonso, R. A. Baragiola, and A. Oliva-Florio, Phys. Rev. B **24**, 4412 (1981).
[25] J. I. Juaristi, R. D. Muino, A. Dubus, and M. Rösler, Phys. Rev. A **68**, 012902 (2003).
[26] G. Lakits, A. Arnau, and H. Winter, Phys. Rev. B **42**, 15

(1990).

[27] J. I. Juaristi, M. Rösler, and F. J. García de Abajo, Phys. Rev. B **58**, 15838 (1998).

[28] F. Aumayr, H. Kurz, D. Schneider, M. A. Briere, J. W. McDonald, C. E. Cunningham, and H. P. Winter, Phys. Rev. Lett. **71**, 1943 (1993).

[29] M. Delaunay, M. Fehringer, R. Geller, D. Hitz, P. Varga, and H. Winter, Phys. Rev. B **35**, 4232 (1987).

[30] H. Kurz, F. Aumayr, C. Lemell, K. Toglhofer, and H. P. Winter, Phys. Rev. A **48**, 2182 (1993).

[31] R. Díez Muiño, A. Salin, N. Stolterfoht, A. Arnau, and P. M. Echenique, Phys. Rev. A **57**, 1126 (1998).

[32] R. Díez Muiño, N. Stolterfoht, A. Arnau, A. Salin, and P. M. Echenique, Phys. Rev. Lett. **76**, 4636 (1996).

[33] J.-P. Briand, B. d'Etat-Ban, D. Schneider, M. A. Briere, V. Decaux, J. W. McDonald, and S. Bardin, Phys. Rev. A **53**, 2194 (1996).

[34] J.-P. Briand *et al.*, Phys. Rev. A **54**, 4136 (1996).

[35] H. Winter, Phys. Rep. **367**, 387 (2002).

[36] R. D. Cowan, *The Theory of Atomic Structure and Spectra* (University of California Press, Berkeley, 1981).

[37] C. P. Bhalla, Phys. Rev. A **8**, 2877 (1973).

[38] J. C. Slater, Phys. Rev. **36**, 57 (1930).

[39] Y. Yamamura and T. Fujii, Nucl. Instrum. Methods Phys. Res. B **153**, 242 (1999).

[40] Y. Yamamura *et al.*, Nucl. Instrum. Methods Phys. Res. B **98**, 400 (1995).

[41] A. Dubus, J.-C. Dehaes, J. P. Ganachaud, A. Hafni, and M. Cailler, Phys. Rev. B **47**, 11056 (1993).

[42] A. Miotello and M. Dapor, Phys. Rev. B **56**, 2241 (1997).

[43] M. P. Seah and W. A. Dench, Surf. Interface Anal. **1**, 2 (1979).

[44] M. Grether, D. Niemann, A. Spieler, and N. Stolterfoht, Phys. Rev. A **56**, 3794 (1997).

[45] L. Wirtz, C. O. Reinhold, C. Lemell, and J. Burgdörfer, Phys. Rev. A **67**, 012903 (2003).

[46] G. Lakits, F. Aumayr, M. Heim, and H. Winter, Phys. Rev. A **42**, 5780 (1990).

[47] J.-P. Briand, S. Thuriez, G. Giardino, G. Borsoni, M. Froment, M. Eddrief, and C. Sebenne, Phys. Rev. Lett. **77**, 1452 (1996).

[48] B. d'Etat, J. P. Briand, G. Ban, L. de Billy, J. P. Desclaux, and P. Briand, Phys. Rev. A **48**, 1098 (1993).

[49] D. R. Penn, Phys. Rev. B **35**, 482 (1987).

[50] L. Folkerts and R. Morgenstern, Europhys. Lett. **13**, 377 (1990).

[51] A. Niehaus, J. Phys B **19**, 2925 (1986).

[52] A. Bárány, G. Astner, H. Cederquist, H. Danaed, S. Huldt, P. Hvelplund, A. Johnson, H. Knudsen, L. Liljeby, and K.-G. Rensfelt, Nucl. Instrum. Methods Phys. Res. B **9**, 397 (1985).

[53] N. Stolterfoht, J. H. Bremer, and R. Díez Muiño, Int. J. Mass Spectrom. **192**, 425 (1999).

[54] H. Kurz, F. Aumayr, H. P. Winter, D. Schneider, M. A. Briere, and J. W. McDonald, Phys. Rev. A **49**, 4693 (1994).

[55] C. Lemell, H. P. Winter, F. Aumayr, J. Burgdörfer, and F. Meyer, Phys. Rev. A **53**, 880 (1996).

[56] H. Winter, C. Auth, R. Schuch, and E. Beebe, Phys. Rev. Lett. **71**, 1939 (1993).

[57] N. Vaeck and J. E. Hansen, J. Phys. B **28**, 3523 (1995).

[58] E. J. McGuire, Phys. Rev. A **3**, 587 (1971).

[59] N. V. Smith, C. T. Chen, and M. Weinert, Phys. Rev. B **40**, 7565 (1989).